ELSEVIER

International Journal of Heat and Fluid Flow 23 (2002) 269–277

International Journal of HEAT AND FLUID FLOW

www.elsevier.com/locate/ijhff

Magnetic field suppression of melt flow in crystal growth ☆

Brian H. Dennis [a], George S. Dulikravich [b,*]

[a] Graduate School of Frontier Sciences, Institute of Environmental Studies, University of Tokyo, 7-3-1 Hongo, Bunkyo-ku, Tokyo 113-8656, Japan
[b] Department of Mechanical and Aerospace Engineering, The University of Texas at Arlington, UTA Box 19018, Arlington, TX 76019, USA

Abstract

The *p*-version least-squares finite element method was used for prediction of solidification from a melt under the influence of an externally applied magnetic field. The computational results indicate significantly different flow-field patterns and thermal fields in the melt and the accrued solid in the cases of full gravity, reduced gravity, and an applied uniform magnetic field. © 2002 Published by Elsevier Science Inc.

1. Introduction

When growing a crystal, such as a semiconductor crystal, it would be ideal to remove the thermally induced melt convection entirely, thus leading to solidification heat transfer by pure conduction. This would be desirable for two reasons. First, if the velocity within the melt region is high, it is more likely that small particles of the crucible wall will be deposited in the crystal (Garandet and Alboussiere, in press). Such contamination dramatically reduces the quality of the solid crystal. Second, for some semiconductors, a dopant is introduced into the melt. It is desirable to achieve a distribution of the dopant in the solid crystal that is as uniform as possible (Hirtz and Ma, 2000). This is easier to realize under the conditions of minimized controlled convection (Hirtz and Ma, 2000).

One way to reduce the convection in the melt region is to perform the crystal growth in a low gravity environment, such as in an Earth-orbiting vehicle. Since semiconductor melts are highly electrically conducting, a more practical approach is to use magnetic and electric fields to suppress the buoyancy induced flows. With such an electromagnetic device, high quality crystals can be produced under full gravity.

Magnetic fields can be used to damp the convection during the directional solidification of electrically conductive melts (Fedoseyev et al., 2001). Computational methods are needed to enhance our understanding of the phenomena occurring during the solidification of semiconductor melts. Effects like the bending of isomagnetic lines and the effects of different crucible shapes on the melt flow are difficult to model analytically and so they may be studied numerically. In addition, numerical simulation can be used together with optimization to determine the distributions of the magnetic field lines and the shape of the crucible that will minimize the convective flow throughout the melt.

The equations for laminar steady-state incompressible Newtonian magnetohydrodynamic flows with the Boussinesq buoyancy approximation (Gray and Giorgini, 1976) can be written in the following non-dimensional form (Hughes and Young, 1966; Dulikravich et al., 1994)

$$\nabla \cdot \mathbf{V}^* = 0 \tag{1}$$

$$\rho^* \mathbf{V}^* \cdot \nabla \mathbf{V}^* - \frac{1}{Re} \nabla \cdot \left(\mu^* \left(\nabla \mathbf{V}^* + (\nabla \mathbf{V}^*)^T \right) \right) + \nabla p^* - \frac{Ht^2}{Re} \mathbf{V}^* \times \mathbf{B}^* \times \mathbf{B}^* - \rho^* Gr \mathbf{k} T^* = 0 \tag{2}$$

$$\rho^* C_p^* \mathbf{V}^* \cdot \nabla T^* - \frac{1}{Pe} \nabla \cdot (k^* \nabla T^*) - \frac{Ht^2 Ec}{Re} (\mathbf{V}^* \times \mathbf{B}^*)^2 = 0 \tag{3}$$

$$\nabla \cdot \mathbf{B}^* = 0 \tag{4}$$

$$\nabla \times \mathbf{B}^* - Rm \mathbf{V}^* \times \mathbf{B}^* = 0 \tag{5}$$

☆ This paper is a revised and expanded version of a paper presented at CHT'01, the Second International Symposium on Advances in Computational Heat Transfer (Palm Cove, Qld., Australia, 20–25 May 2001), the proceedings of which were published by Begell House, Inc.

* Corresponding author. Tel.: +1-817-272-7376; fax: +1-817-272-5010.

E-mail address: gsd@mae.uta.edu (G.S. Dulikravich).

0142-727X/02/$ - see front matter © 2002 Published by Elsevier Science Inc.
PII: S0142-727X(02)00174-1

where $\mathbf{V}^*$ is the fluid velocity, ρ^* is the fluid density, p^* is the hydrodynamic pressure, μ^* is the temperature dependent coefficient of viscosity, $\mathbf{B}^*$ is the magnetic flux density. Only the presence of a steady magnetic field is considered here so the equations and terms in Maxwell's equations relating to the electric field are omitted. The non-dimensional variables are defined as $\mathbf{V}^* = \mathbf{V}U_0^{-1}$, $\mathbf{B}^* = \mathbf{B}B_0^{-1}$, $p^* = p\rho_0^{-1}U_0^{-2}$, $x^* = xL_0^{-1}$, $y^* = yL_0^{-1}$, $\rho^* = \rho\rho_0^{-1}$, $\mu^* = \mu\mu_0^{-1}$, $C_p^* = C_pC_{p0}^{-1}$, and $T^* = (T - T_{\text{cold}})/\Delta T_0$. The vector $\mathbf{k}$ is the unit normal in the y-direction. The temperature is non-dimensionalized with a temperature difference, ΔT_0, where $\Delta T_0 = T_{\text{hot}} - T_{\text{cold}}$. The non-dimensional numbers are given by

Reynolds number: $$Re = \frac{\rho_0 U_0 L_0}{\mu_0}$$

Grashof number: $$Gr = \frac{\Delta T_0 \beta_0 g_0 L_0}{U_0^2}$$

Peclet number: $$Pe = \frac{L_0 U_0 \rho_0 C_{p0}}{k_0}$$

Hartmann number: $$Ht = L_0 B_0 \sqrt{\frac{\sigma_0}{\mu_0}}$$

Magnetic Reynolds number: $$Rm = \eta_0 \sigma_0 U_0 L_0$$

Eckert number: $$Ec = \frac{U_0^2}{C_{p0}\Delta T_0}$$

where C_{p0} is the specific heat, k_0 is the heat conductivity coefficient, β_0 is the volumetric thermal expansion coefficient, g_0 is the acceleration of gravity, η_0 is the magnetic permeability coefficient, and σ_0 is the electrical conductivity of the fluid.

The following dimensionless numbers are useful for buoyancy driven flows:

Rayleigh number $$Ra = \frac{\rho_0^2 C_{p0} \beta_0 g_0 L_0^3 \Delta T_0}{k_0 \mu_0}$$

Prandtl number $$Pr = \frac{\mu_0 C_{p0}}{k_0}$$

If one specifies the values of Ra for a given fluid with a known value of Pr then the Reynolds number and the Peclet number are determined by the following (Tang and Tsang, 1993):

$$Re = \sqrt{\frac{Ra}{Pr}} \tag{6}$$

$$Pe = \sqrt{RaPr} \tag{7}$$

This leads to the formula for the reference speed, U_0.

$$U_0 = \sqrt{\beta_0 g_0 L_0 \Delta T_0} \tag{8}$$

Table 1
Parameters for MHD silicon crystal growth problem

Density of the melt	ρ_l (kg m^{-3})	2550.0
Density of the solid	ρ_s (kg m^{-3})	2330.0
Length of the container	Length (m)	0.10
Heat conductivity of the melt	k_l (W kg^{-1} K^{-1})	64.0
Heat conductivity of the solid	k_s (W kg^{-1} K^{-1})	22.0
Liquidus temperature	T_l (K)	1685.0
Solidus temperature	T_s (K)	1681.0
Specific heat of the melt	C_pl (J kg^{-1} K^{-1})	1059.0
Specific heat of the solid	C_ps (J kg^{-1} K^{-1})	1038.0
Viscosity of the melt	μ (kg m^{-1} s^{-1})	0.0007
Electric conductivity	σ (Ω^{-1} m^{-1})	4.3×10^4
Latent heat of phase change	L (J kg^{-1})	1.8×10^6
Thermal expansion coefficient	β (K^{-1})	1.4×10^{-4}

which then requires that $Gr = 1$. One avoids explicitly specifying the reference velocity, U_0, by defining the Reynolds, Peclet, and Grashof numbers in this way.

In this paper, the growth of a silicon crystal under an applied magnetic field has been simulated with the p-version of the least-squares finite element method (LSFEM) (Jiang, 1998; Bochev, 1997) for magnetohydrodynamics (MHD) (Dulikravich, 1999; Dennis and Dulikravich, 2000, 2001). The solidification is modeled by using temperature dependent properties. The material properties for silicon are given in Table 1. Here L is the latent heat of liquid/solid phase change. The subscripts l and s refer to the liquid and solid properties, respectively. In the mushy region (where $T_l > T > T_s$), the density, specific heat, latent heat, and the viscosity were taken as linear functions of temperature.

$$f = \frac{T - T_s}{T_l - T_s} \tag{9}$$

$$\rho = f\rho_l + (1 - f)\rho_s \tag{10}$$

$$\mu = f\mu_l + (1 - f)\mu_s \tag{11}$$

$$C_p = fC_{pl} + (1 - f)C_{ps} \tag{12}$$

The solid regions are modeled as a melt with a high viscosity ($\mu_s = 10^3$ kg m^{-1} s^{-1}) (Dulikravich et al., 1994). Consequently, the computed velocities in the solid regions are not identically zero, but are extremely small compared to the velocities in the melt. This formulation allows one code to simultaneously simulate heat transfer through solid, melt, and mushy regions.

The effect of the latent heat, L, is included by using an enthalpy method (Morgan et al., 1977). Typically, the effect of the latent heat can be included in a numerical simulation by allowing a rapid variation in the heat capacity in the mushy region. This direct evaluation leads to satisfactory numerical integrations only if the curve of the heat capacity against the temperature does not possess sharp peaks. If the mushy region is completely contained within a single element, there is a chance that it may not fall on an integration point and

hence the latent heat will not be accounted for in the integration process. A better approach is to work with enthalpy, H, which is a smooth function even in the phase change zone. The effective heat capacity can be evaluated without missing the peaks due to the latent heat. The relation

$$\rho C_p = \frac{\mathrm{d}H}{\mathrm{d}T} \tag{13}$$

is approximated by

$$\rho C_p \approx \frac{\sqrt{(\partial H/\partial x)^2 + (\partial H/\partial y)^2}}{\sqrt{(\partial T/\partial x)^2 + (\partial T/\partial y)^2}} \tag{14}$$

in an attempt to avoid the possibility of missing the peak values ρC_p during the numerical integration procedure.

2. Numerical method

The p-version LSFEM (Jiang and Sonnad, 1994) was implemented in this work. Details have been published recently by the authors (Dennis, 2000).

The LSFEM can be formed for the general linear first-order system of partial differential equations written as

$$[L]\mathbf{u} = \mathbf{f} \tag{15}$$

where the first order operator is defined in a two-dimensional space as

$$[L] = [A_1]\frac{\partial}{\partial x} + [A_2]\frac{\partial}{\partial y} + [A_3] \tag{16}$$

The residual of the system is represented by $\mathbf{R}$.

$$\mathbf{R}(\mathbf{u}) = [L]\mathbf{u} - \mathbf{f} \tag{17}$$

We now define the following least squares functional $I(\mathbf{u})$ over the domain Ω

$$I(\mathbf{u}) = \int_\Omega \mathbf{R}(\mathbf{u})^T \cdot \mathbf{R}(\mathbf{u})\,\mathrm{d}x\,\mathrm{d}y \tag{18}$$

The weak statement is then obtained by taking the variation of I with respect to $\mathbf{u}$ and setting the result equal to zero.

$$\delta I(\mathbf{u}) = \int_\Omega ([L]\delta\mathbf{u})([L]\mathbf{u} - \mathbf{f})\,\mathrm{d}x\,\mathrm{d}y = 0 \tag{19}$$

Using equal order shape functions, ϕ_i, for all unknowns, the vector of unknowns $\mathbf{u}$ can be written as

$$\mathbf{u} = \sum_{i=1}^{n} \phi_i \{u_1, u_2, u_3, \ldots, u_m\}_i^T \tag{20}$$

where $\{u_1, u_2, u_3, \ldots, u_m\}_i$ are the nodal values at the ith node of the finite element. Here, m is the number of unknowns at each node and n is the number of nodes per element. Introducing the above approximation for $\mathbf{u}$ into the weak statement leads to a linear system of algebraic equations

$$[K]\mathbf{U} = \mathbf{F} \tag{21}$$

where $[K]$ is the stiffness matrix, $\mathbf{U}$ is the vector of unknowns, and $\mathbf{F}$ is the force vector. It should be noted that with this formulation $[K]$ is always symmetric and positive definite.

Use of the LSFEM for systems of equations that contain higher order derivatives is usually difficult due to the higher continuity restrictions imposed on the approximation functions. For this reason, it is usually more convenient to transform the system into an equivalent first order form before applying the LSFEM. For the case of MHD, the second order derivatives are transformed by introducing vorticity, ω, and heat flux, $\mathbf{q}$, as additional unknowns. The final coupled system after eliminating asterisk symbols becomes

$$\nabla \cdot \mathbf{V} = 0 \tag{22}$$

$$\rho\mathbf{V}\cdot\nabla\mathbf{V} + \frac{1}{Re}(\mu\nabla\times\omega + (\nabla\mathbf{V} + (\nabla\mathbf{V})^T)\cdot\nabla\mu) + \nabla p - \frac{Ht^2}{Re}\mathbf{V}\times\mathbf{B}\times\mathbf{B} - \rho Gr\,\mathbf{k}T = 0 \tag{23}$$

$$\omega - \nabla\times\mathbf{V} = 0 \tag{24}$$

$$\rho C_p\mathbf{V}\cdot\nabla T + \frac{1}{Pe}\nabla\cdot\mathbf{q} - \frac{Ht^2 Ec}{Re}(\mathbf{v}\times\mathbf{B})^2 = 0 \tag{25}$$

$$\mathbf{q} + k\nabla T = 0 \tag{26}$$

$$\nabla\times\mathbf{q} = 0 \tag{27}$$

$$\nabla\cdot\mathbf{B} = 0 \tag{28}$$

$$\nabla\times\mathbf{B} - Rm\mathbf{V}\times\mathbf{B} = 0 \tag{29}$$

It should be noted that a curl-free condition on the heat flux vector field, $\mathbf{q}$, appears in the first-order form. It was shown by Jiang and Povinelli (Jiang and Povinelli, 1993) that the presence of this condition is required for achieving optimal convergence rates for the heat flux vector when Poisson's equation was solved with the LSFEM. It was also shown by Jiang and Povinelli (Jiang and Povinelli, 1993) that the inclusion of the curl-free condition does not produce an over-determined system of equations.

We consider a two-dimensional problem only and write the above system in the general form of a first-order system (15). Although the LSFEM is perfectly capable of treating the entire system written in (22)–(29), it has been found that for low values of Rm it is more economical to solve the thermal-fluid and magnetic field equations separately. Here, a general form first-order system is written for the thermal-fluid system (22)–(24) and denoted by the superscript fluid. A separate first-order system is also written in general form for the

magnetic field equations (25)–(29) and is denoted by the superscript mag. In addition, the non-linear convective terms in the fluid flow equations are linearized with Newton's method leading to a system suitable for treatment with the LSFEM described previously. Non-linear terms due to temperature dependent material properties are linearized by using the property value from the previous iteration.

$$[A_1^{\text{fluid}}] = \begin{bmatrix} 1 & 0 & 0 & 0 & 0 & 0 & 0 \\ \rho_0 u_0 + 2\frac{\partial \mu_0}{\partial x} & \frac{\partial \mu_0}{\partial y} & 1 & 0 & 0 & 0 & 0 \\ 0 & \rho_0 u_0 + \frac{\partial \mu_0}{\partial x} & 0 & -\frac{1}{Re} & 0 & 0 & 0 \\ 0 & -1 & 0 & 0 & 0 & 0 & 0 \\ 0 & 0 & 0 & 0 & \rho_0 C_{p0} u_0 & \frac{1}{Pe} & 0 \\ 0 & 0 & 0 & 0 & k_0 & 0 & 0 \\ 0 & 0 & 0 & 0 & 0 & 0 & 0 \\ 0 & 0 & 0 & 0 & 0 & 0 & -1 \end{bmatrix},$$

$$[A_2^{\text{fluid}}] = \begin{bmatrix} 0 & 1 & 0 & 0 & 0 & 0 & 0 \\ \rho_0 v_0 + \frac{\partial \mu_0}{\partial y} & 0 & 0 & \frac{1}{Re} & 0 & 0 & 0 \\ \frac{\partial \mu_0}{\partial x} & \rho_0 v_0 + 2\frac{\partial \mu_0}{\partial y} & 1 & 0 & 0 & 0 & 0 \\ 1 & 0 & 0 & 0 & 0 & 0 & 0 \\ 0 & 0 & 0 & 0 & \rho_0 C_{p0} v_0 & 0 & \frac{1}{Pe} \\ 0 & 0 & 0 & 0 & 0 & 0 & 0 \\ 0 & 0 & 0 & 0 & k_0 & 0 & 0 \\ 0 & 0 & 0 & 0 & 0 & 1 & 0 \end{bmatrix},$$

$$[A_3^{\text{fluid}}] = \begin{bmatrix} 0 & 0 & 0 & 0 & 0 & 0 \\ \frac{Ht^2}{Re} B_{y0}^2 + \rho_0 \frac{\partial u_0}{\partial x} & -\frac{Ht^2}{Re} B_{x0} B_{y0} + \rho_0 \frac{\partial u_0}{\partial y} & 0 & 0 & -k_x \rho_0 Gr & 0 & 0 \\ -\frac{Ht^2}{Re} B_{x0} B_{y0} + \rho_0 \frac{\partial v_0}{\partial x} & \frac{Ht^2}{Re} B_{x0}^2 + \rho_0 \frac{\partial v_0}{\partial y} & 0 & 0 & -k_y \rho_0 Gr & 0 & 0 \\ 0 & 0 & 0 & 1 & 0 & 0 & 0 \\ \rho_0 C_{p0} \frac{\partial T_0}{\partial x} & \rho_0 C_{p0} \frac{\partial T_0}{\partial y} & 0 & 0 & 0 & 0 & 0 \\ 0 & 0 & 0 & 0 & 0 & 1 & 0 \\ 0 & 0 & 0 & 0 & 0 & 0 & 1 \\ 0 & 0 & 0 & 0 & 0 & 0 & 0 \end{bmatrix}, \tag{30}$$

$$\mathbf{f}^{\text{fluid}} = \begin{Bmatrix} 0 \\ \rho_0 (u_0 \frac{\partial u_0}{\partial x} + v_0 \frac{\partial u_0}{\partial y}) \\ \rho_0 (u_0 \frac{\partial v_0}{\partial x} + v_0 \frac{\partial v_0}{\partial y}) \\ 0 \\ \rho_0 C_{p0} (u_0 \frac{\partial T_0}{\partial x} + v_0 \frac{\partial T_0}{\partial y}) + \frac{Ht^2 Ec}{Re} (u_0 B_{y0} - v_0 B_{x0})^2 \\ 0 \\ 0 \\ 0 \end{Bmatrix},$$

$$\mathbf{u}^{\text{fluid}} = \begin{Bmatrix} u \\ v \\ p \\ \omega \\ T \\ q_x \\ q_y \end{Bmatrix} \tag{31}$$

$$[A_1^{\text{mag}}] = \begin{bmatrix} 1 & 0 \\ 0 & 1 \end{bmatrix}, \quad [A_2^{\text{mag}}] = \begin{bmatrix} 0 & 1 \\ -1 & 0 \end{bmatrix},$$
$$[A_3^{\text{mag}}] = \begin{bmatrix} 0 & 0 \\ Rm\, v_0 & -Rm\, u_0 \end{bmatrix}, \quad \mathbf{f}^{\text{mag}} = \begin{Bmatrix} 0 \\ 0 \end{Bmatrix}, \tag{32}$$
$$\mathbf{u}^{\text{mag}} = \begin{Bmatrix} B_x \\ B_y \end{Bmatrix}$$

The solution to the above systems can be found by solving the linear systems in an iterative manner until a desired convergence level is achieved. For many engineering problems involving MHD, the value of $Rm \ll 1$, meaning that induced magnetic field is small relative to the applied magnetic field. Assuming small Rm and uniform electrical conductivity throughout the melt, the solution for the magnetic field can be determined that is independent of the thermal-fluid solution. Here, quantities taken from the previous iteration are designated with the subscript 0.

The p-version of LSFEM was used to compute all results reported here. In the p-version LSFEM, a relatively coarse mesh is used. The order of the approximation function is increased, or enriched, until the desired level of convergence is obtained. In this case, the size of the mesh is fixed and the order of the approximation can be increased uniformly across the mesh. For problems with smooth solutions, the p-version of LSFEM converges to the exact solution at an exponential rate as the number of unknowns is increased by uniform enrichment of the element approximation functions. The more common h-type LSFEM is based on low order elements. It converges at a fixed rate as the number of unknowns is increased by way of uniform grid refinement.

Most p-type expansions can be categorized as either nodal or modal expansions. In nodal expansion, the unknowns become the value of the function at the nodes of the finite element. In a modal expansion, the unknowns are coefficients that may have no obvious physical meaning as they do in the nodal expansion case. This makes the imposition of boundary conditions with a non-linear spatial distribution less direct than in the nodal expansion case.

The one-dimensional approximation function is given as

$$u(x) = \sum_{p}^{P+1} \Phi_p(x) \hat{a}_p \tag{33}$$

where $\Phi_p(x)$ are the p-type expansion basis functions and $\hat{a}_p$ are constant coefficients.

A one-dimensional modal basis can be written in general form as

$$\Phi_p(x) = L_p(x), \quad p = 0, \ldots, P \tag{34}$$

Here the p-type modal basis function is composed of $P+1$ polynomials, L_p, where each polynomial is of order p. The modal basis functions of this type are called hierarchical modal expansions. This term stems from the observation that an expansion set of order P is contained within the expansion set of order $P+1$. The higher order expansion sets are built from the lower order expansion sets. This allows for efficient programming and computation of the approximation functions,

particularly if adaptive enrichment strategies are used. Once the *p*-type expansion is developed in one dimension, approximation functions for quadrilateral and hexahedral elements can be constructed easily by using tensor products of the approximation function in one-dimensional space.

The *p*-type finite elements used in this research were developed using hierarchical basis functions based on Jacobi polynomials (Karniadakis and Sherwin, 1999). The Jacobi polynomials are a set of orthogonal polynomials that are a superset of well-known expansions such as Legendre or Chebyshev polynomials. Use of Jacobi polynomials results in stiffness matrices that are relatively sparse and well conditioned compared with matrices constructed using nodal expansions such as the popular Lagrange polynomials (Karniadakis and Sherwin, 1999).

The sparse linear systems were solved by either direct sparse LU factorization or by iterative methods. Two iterative methods were implemented in the software; one based on a Jacobi preconditioned conjugate gradient, and another based on a multigrid-like technique that uses the hierarchy of basis functions instead of a hierarchy of finer grids. The method was implemented in an object-oriented fashion using the C++ programming language. The software has been tested against analytic solutions and experimental data for Navier–Stokes equations and for single-phase laminar incompressible steady channel flows through transverse electric and magnetic fields, for shear-driven cavity flows, buoyancy-driven cavity flows, and flow over a backward-facing step (Dennis, 2000).

3. Verification of accuracy

The accuracy of the LSFEM for MHD was tested against known analytic solutions for Poiseuille–Hartmann flow. The Poiseuille–Hartmann flow is a one-dimensional flow of a conducting and viscous fluid between two stationary plates with a uniform external magnetic field applied orthogonal to the plates. An analytical solution to the equations governing steady MHD can be found for this case (Hughes and Young, 1966; Cramer and Pai, 1973).

The Hartmann flow problem has been computed using the *p*-version LSFEM method for MHD. A mesh composed of only four quadrilateral elements was used and is shown in Fig. 3. A uniform *p*-level of $P = 8$ was used for all cases. Fig. 1 shows the change in the *u* velocity for different values of Hartmann number for both the analytic solution and the computed solution. Fig. 2 shows the change in the *x*-component of the magnetic field for different values of Hartmann number for both the analytic solution and the computed solution. Larger values of Hartmann number, *Ht*, correspond to larger magnetic field strengths. Excellent agreement is obtained between the computed and analytic solutions for the range of Hartmann numbers. The Fig. 4 shows the accuracy of the method versus the number of unknowns. The *h*-type method uses parabolic elements and the mesh is successively refined by uniformly dividing each element into four smaller elements.

The *p*-type method uses the initial mesh and successively increases the *p*-level for each element. The initial mesh contained four elements as shown in Fig. 3. The results clearly show that for the same number of degrees of freedom (DOF), the *p*-type elements are much more

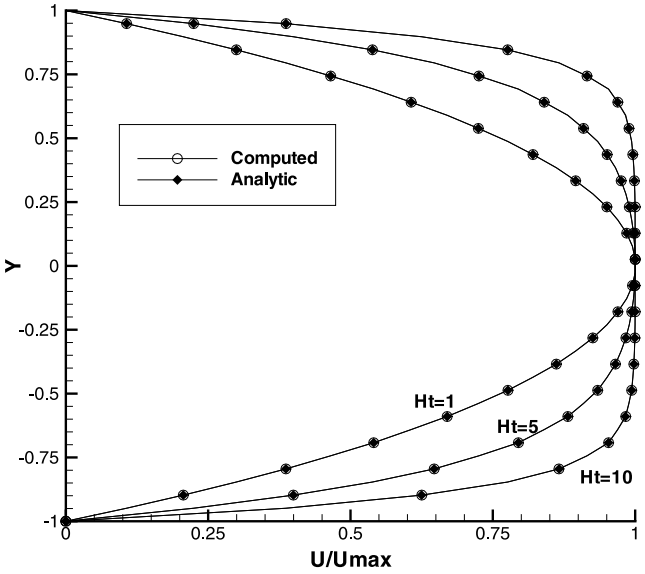

Fig. 1. Computed velocity profiles for Hartmann flow for various values of *Ht*.

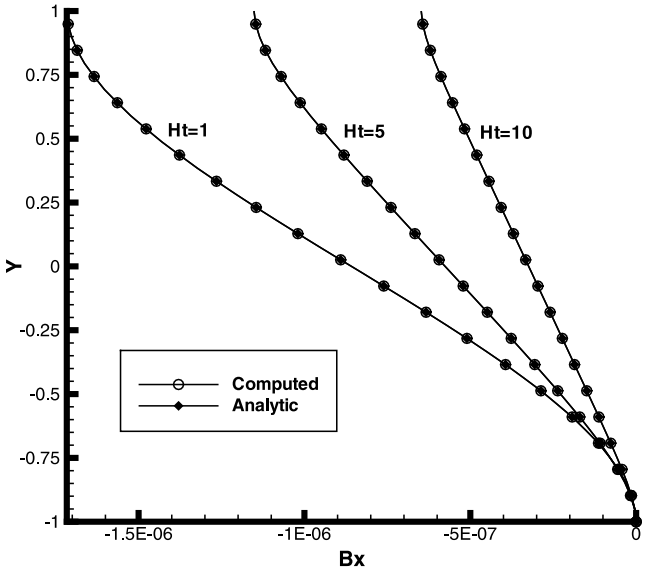

Fig. 2. Computed *x*-component of flow induced magnetic field for Hartmann flow for various values of *Ht*.

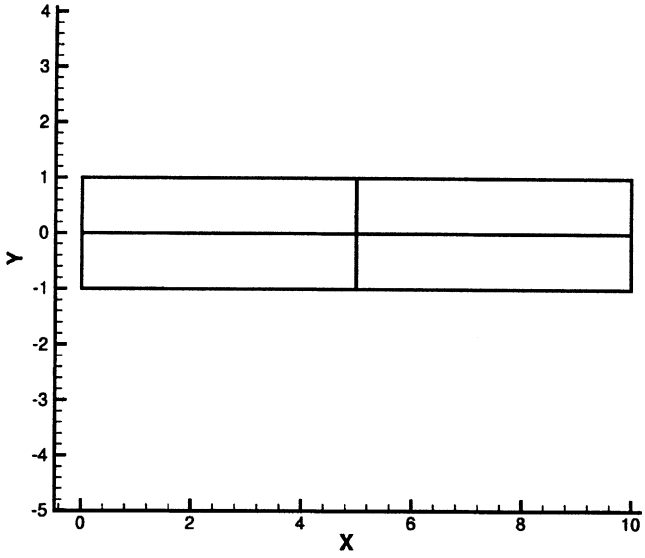

Fig. 3. Mesh used for the Hartmann flow test problem.

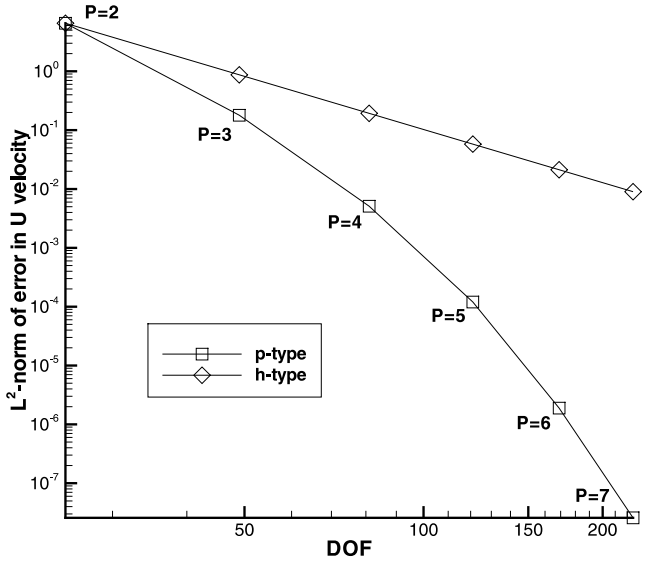

Fig. 4. Convergence rate for p and h type refinement for Hartmann flow problem.

accurate. However, this does not always mean that the p-type method is more efficient computationally. For the same numbers of unknowns, the p-type mesh results in a denser matrix than the corresponding h-type mesh.

4. Numerical results

The solidification of a silicon melt in a square container both with and without an applied vertical magnetic field was simulated numerically. The container sides had a length of 0.1 m. The side walls were thermally insulated. A slightly parabolic temperature profile was applied to the bottom of the container to simulate non-uniform heating of the melt. The temperature at the center of the bottom wall was 1688.0 K and the temperature at the bottom corners was set to 1686.0 K. A uniform temperature of 1676.0 K was applied to the top wall so that the solidification originates on the top wall of the container. A no-slip condition for velocity was enforced on all four walls of the container. A quadrilateral mesh with 121 elements with a p-level of $P = 6$ was used for all cases. The mesh is shown in Fig. 5. A uniform vertical magnetic field was applied by assuming magnets on the top and bottom walls while using a perfect conductor on the side walls.

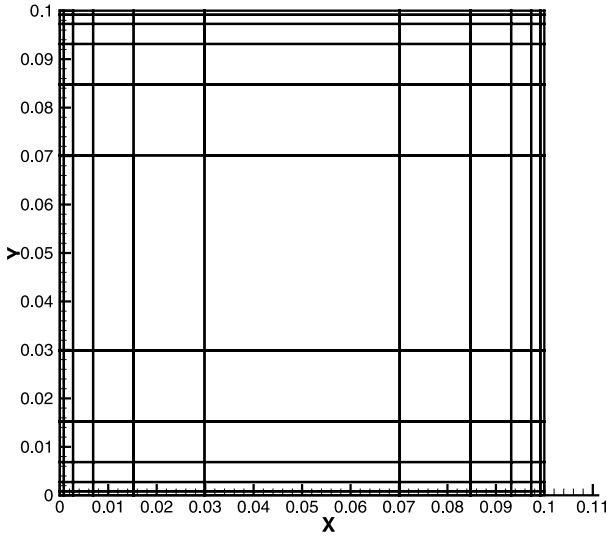

Fig. 5. Mesh from crystal growth problem.

Three test cases have been simulated numerically. In all cases gravity acts in the y-direction and is therefore aligned with the magnetic field. In all the cases the steady-state solution to the equations governing MHD with heat transfer is predicted. The relevant non-dimensional and dimensional parameters for these test cases are shown in Table 2.

The first case uses full gravity, $g = 9.81\ \mathrm{m\,s^{-2}}$ with an applied magnetic field strength of $B_0 = 0.0$ T. Fig. 8 shows the computed streamlines within the melt region. Two pairs of counter-rotating vortices are present within the melt region. Fig. 7 shows the computed velocity magnitude within the melt region. The maximum velocity is $0.00212\ \mathrm{m\,s^{-1}}$ and occurs at approximately $x = 0.05$ m and $y = 0.015$ m. The computed temperature distribution is shown in Fig. 6. The motion of the melt results in a temperature distribution that is quite different from that obtained under pure diffusion.

The second case uses reduced gravity, $g = 0.10\ \mathrm{m\,s^{-2}}$, with an applied magnetic field strength of $B_0 = 0.0$ T. Such an environment would exist if the crystal were grown in a low orbit Earth-orbiting satellite. Fig. 9 shows the computed streamlines within the melt region. Two pairs of counter-rotating vortices are present within the melt region. In this case, the vortices are

Table 2
Relevant dimensional and non-dimensional parameters for the three test cases

Test case	g (m s^{-2})	B_0 (T)	Re	Pe	Ra	Pr	Ht
1	9.81	0.0	4269.14	49.4487	211103	0.01158	0.0
2	0.1	0.0	431.029	4.99252	2151.92	0.01158	0.0
3	9.81	1.0	4269.14	49.4487	211103	0.01158	783.764

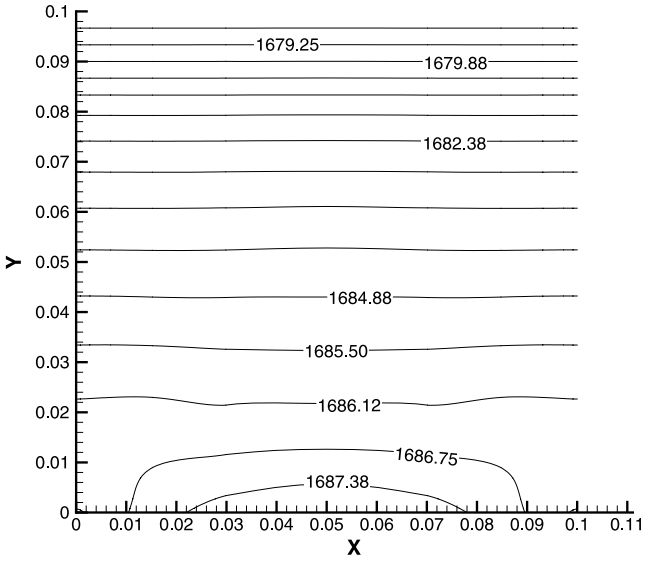

Fig. 6. Computed temperature contours for $g = 9.81$ m s^{-2} and $B_0 = 0.0$ T.

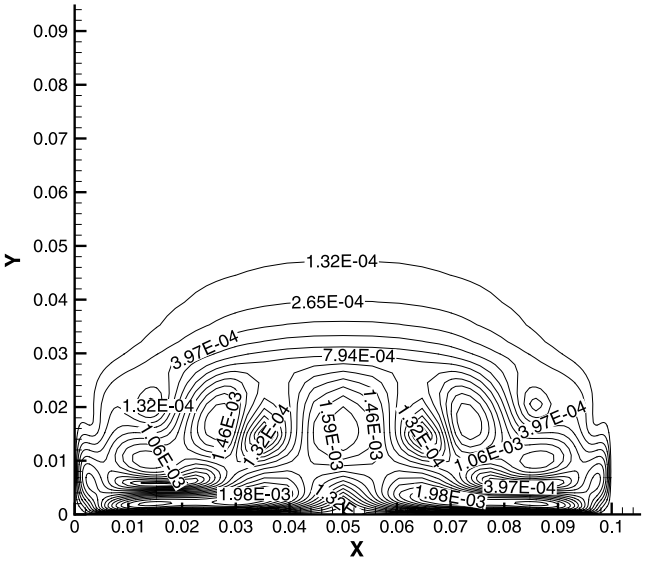

Fig. 7. Computed velocity magnitude for $g = 9.81$ m s^{-2} and $B_0 = 0.0$ T.

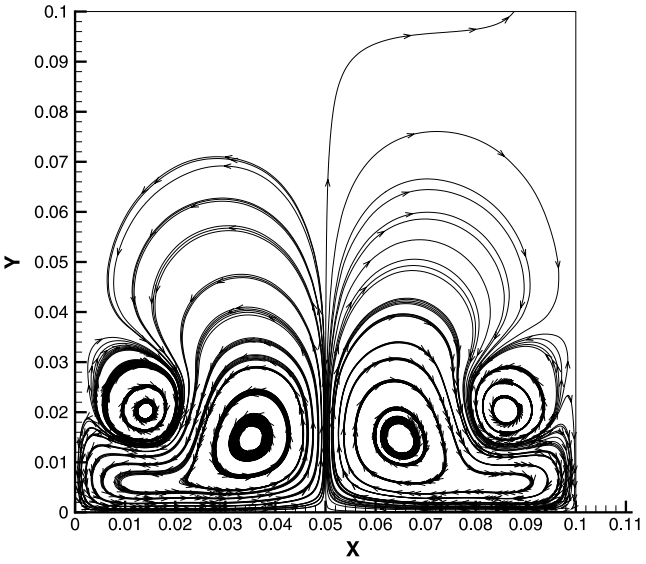

Fig. 8. Computed streamlines for $g = 9.81$ m s^{-2} and $B_0 = 0.0$ T.

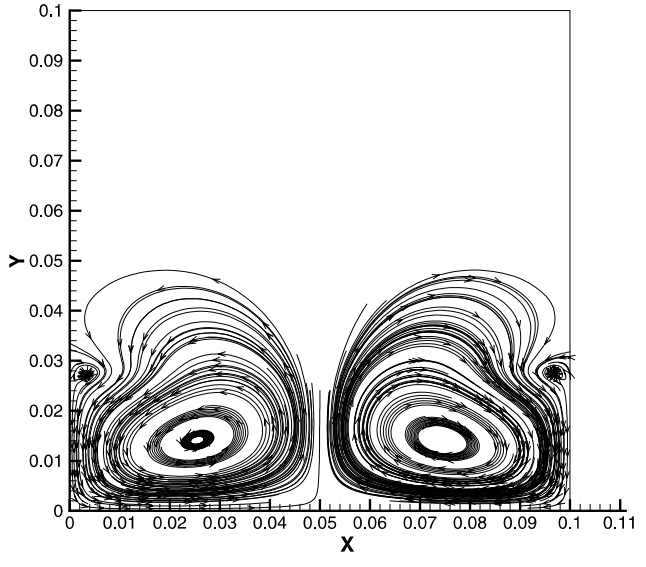

Fig. 9. Computed streamlines for $g = 0.01$ m s^{-2} and $B_0 = 0.0$ T.

weaker than in the first case. Fig. 11 shows the computed velocity magnitude within the melt region. The maximum velocity is 0.000172 m s^{-1} and occurs at approximately $x = 0.05$ m and $y = 0.015$ m. The computed temperature distribution is shown in Fig. 10. The temperature distribution is very similar to that obtained under pure diffusion.

The last case uses full gravity, $g = 9.81$ m s^{-2} with an applied magnetic field strength of $B_0 = 1.0$ T. Fig. 12 shows the computed streamlines within the melt region. Only one pair of counter-rotating vortices is present

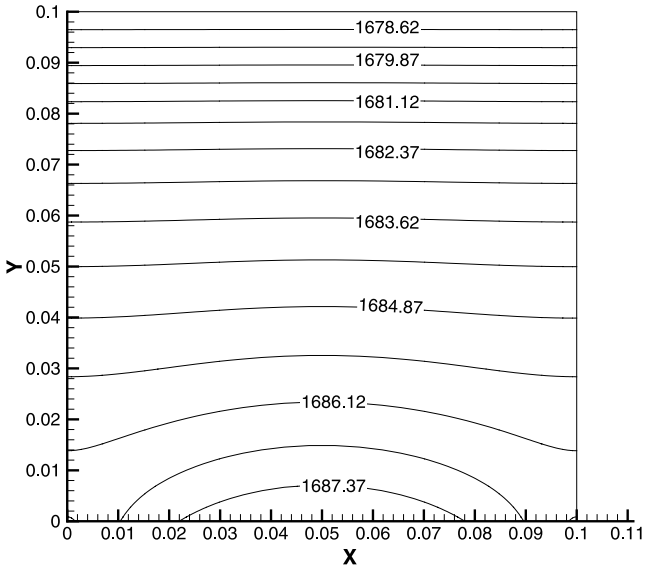

Fig. 10. Computed temperature contours for $g = 0.01\ \mathrm{m\,s^{-2}}$ and $B_0 = 0.0$ T.

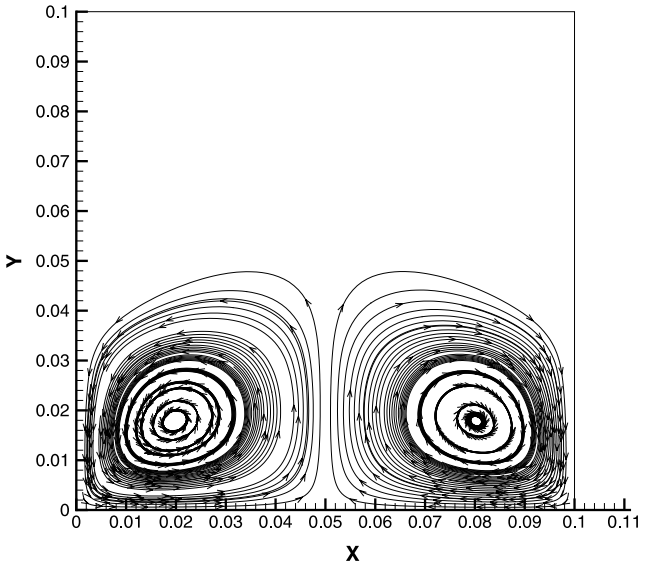

Fig. 12. Computed streamlines for $g = 9.81\ \mathrm{m\,s^{-2}}$ and $B_0 = 1.0$ T.

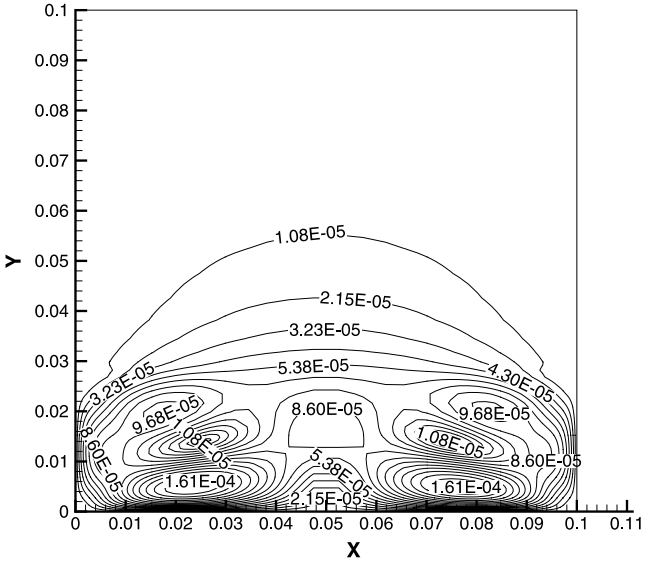

Fig. 11. Computed velocity magnitude for $g = 0.01\ \mathrm{m\,s^{-2}}$ and $B_0 = 0.0$ T.

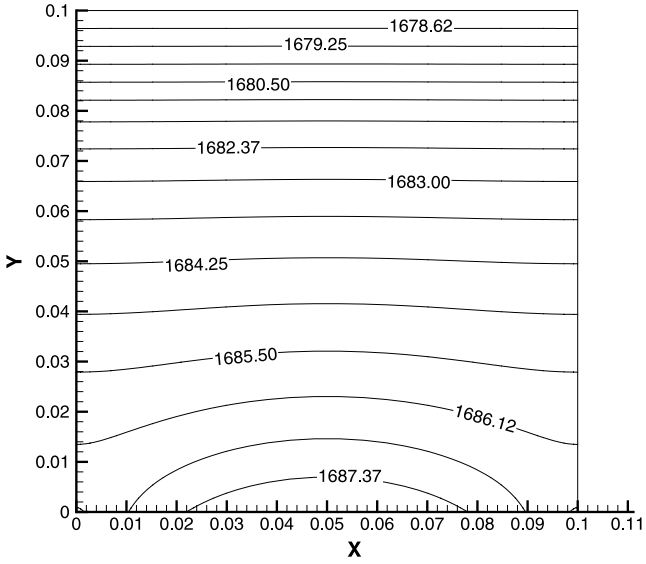

Fig. 13. Computed temperature contours for $g = 9.81\ \mathrm{m\,s^{-2}}$ and $B_0 = 1.0$ T.

within the melt region. Thus, the magnetic field has completely suppressed the secondary vortices that were present in the cases without the magnetic field. Fig. 14 shows the computed velocity magnitudes within the melt region. The maximum velocity is only 0.0000434 $\mathrm{m\,s^{-1}}$ and occurs at approximately $x = 0.05$ m and $y = 0.018$ m. This location is slightly higher than in the previous test cases. In this case the strong vertical magnetic field acts as a resistance to the horizontal components of the velocity field due to the Lorentz force. This results in a suppression of the circulation within the melt region. The computed temperature distribution is shown in Fig. 13. The temperature distribution is very similar to that obtained under pure diffusion. This case demonstrates that thermal buoyancy-induced flow intensity can be significantly reduced through the use of applied magnetic fields, even under full gravity. In the applied magnetic field case the dominant mode of heat transfer is conduction whereas in the full gravity case with no magnetic field the heat transfer is carried out by both conduction and thermal convection.

It should be noted that in this analysis it is assumed that the solid and the liquid regions have the same electrical conductivity. In the real case, the electrical

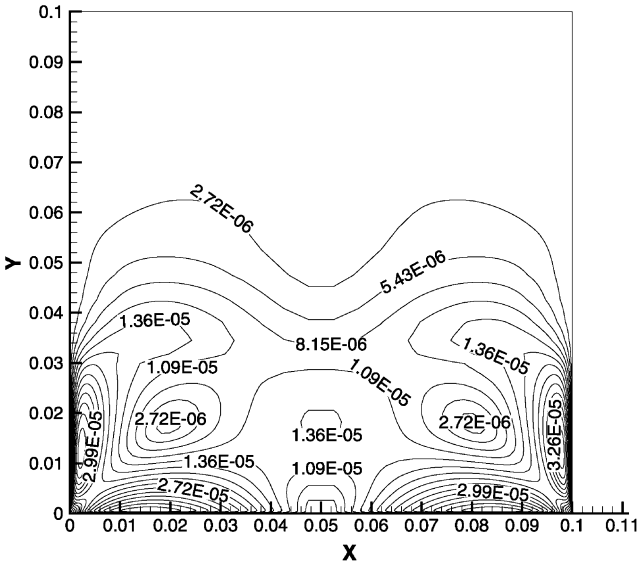

Fig. 14. Computed velocity magnitude for $g = 9.81\ \mathrm{m\,s^{-2}}$ and $B_0 = 1.0$ T.

conductivity may vary significantly between the solid and liquid phases. This change in conductivity would result in the bending of the magnetic field lines through the mushy region (Fedoseyev et al., 2001). The present LSFEM algorithm would need to be modified to include a front tracking algorithm in order to accurately account for this effect. Also, problems with strong thermal buoyancy are usually three-dimensional flows. Therefore, more physically meaningful results could be obtained with a fully three-dimensional or axisymmetric simulation.

5. Conclusions and recommendations

The *p*-version LSFEM was successfully used for the prediction of solidification from a melt under an externally applied uniform magnetic field. The computational results indicate significantly different flow-field patterns and thermal fields in the melt and the accrued solid in the cases of full gravity, reduced gravity, and an applied uniform magnetic field. Although the magnetic field significantly reduces the velocity of the flow within the melt, the crystal may still be slightly contaminated. It is possible that a uniform magnetic field much stronger than 1.0 T may be required to completely eliminate the motion within the melt. Such magnets require superconducting ceramics and are costly to maintain. However, it may be possible to use the current LSFEM based software for MHD together with numerical optimization software to optimize the shape of the container as well as the distribution of the magnetic field along the container wall. Such optimized configurations may locally eliminate motion in the melt while using lower strength magnets.

References

Bochev, P.B., 1997. Analysis of least-squares finite element methods for Navier-Stokes equations. SIAM Journal of Numerical Analysis 34 (5), 1817–1844.

Cramer, K.R., Pai, S., 1973. Magnetofluid Dynamics for Engineers and Applied Physicists. Scripta, Washington, DC.

Dennis, B.H., 2000. Simulation and Optimization of Electromagneto-hydrodynamic Flows. PhD thesis, Pennsylvania State University, University Park, PA.

Dennis, B.H., Dulikravich, G.S., 2000. Simulation of magnetohydrodynamics with conjugate heat transfer. In: Onate, E. (Ed.), European Congress on Computational Methods in Applied Sciences and Engineering. Barcelona, Spain, 11–14 September.

Dennis, B.H., Dulikravich, G.S., 2001. Optimization of magneto-hydrodynamic control of diffuser flows using micro-genetic algorithm and least squares finite elements. Journal of Finite Elements in Finite Elements in Design 37, 349–363.

Dulikravich, G.S., 1999. Electro-magneto-hydrodynamics and solidification. In: Siginer, D.A., Kee, D.D., Chhabra, R.P. (Eds.), Advances in Flow and Rheology of Non-Newtonian Fluids, Part B, volume 8 of Rheology Series. Elsevier Publishers, Amsterdam, pp. 677–716 (Chapter 9).

Dulikravich, G.S., Ahuja, V., Lee, S., 1994. Modeling three-dimensional solidification with magnetic fields and reduced gravity. International Journal of Heat and Mass Transfer 37 (5), 837–853.

Fedoseyev, A.I., Kansa, E.J., Marin, C., Ostrogorsky, A.G., 2001. Magnetic field suppression of semiconductor melt flow in crystal growth: comparison of three methods for numerical modeling. Japanese CFD Journal (9), 325–333.

Garandet, J.P., Alboussiere, T. Bridgman Growth: Modeling and Experiments. Pergamon Press, Oxford, in press.

Gray, D.D., Giorgini, A., 1976. The validity of the Boussinesq approximation for liquids and gases. International Journal of Heat and Mass Transfer 19, 175–189.

Hirtz, J.M., Ma, N., 2000. Dopant transport during semiconductor crystal growth: axial versus transverse magnetic fields. Journal of Crystal Growth 210, 554–572.

Hughes, W.F., Young, F.J., 1966. The Electromagnetodynamics of Fluids. John Wiley and Sons, New York.

Jiang, B.-N., 1998. The Least-Squares Finite Element Method. Springer-Verlag, Berlin.

Jiang, B.-N., Povinelli, L.A., 1993. Optimal least-square finite element method for elliptic problems. Computer Methods in Applied Mechanics and Engineering 102, 199–212.

Jiang, B.-N., Sonnad, V., 1994. Least-squares solution of incompressible Navier–Stokes equations with the *p*-version of finite elements. Computational Mechanics 15, 129–136.

Karniadakis, G.E., Sherwin, S.J., 1999. Spectral/hp Element Methods for CFD. Oxford University Press, New York.

Morgan, K., Lewis, R.W., Zienkiewicz, O.C., 1977. An improved algorithm for heat conduction and problems with phase change. International Journal for Numerical Methods in Engineering, 1191–1195.

Tang, L.Q., Tsang, T.H., 1993. A least-squares finite element method for time-dependant incompressible flows with thermal convection. International Journal for Numerical Methods in Fluids 17, 271–289.